Title: Spatial point pattern analysis identifies mechanisms shaping the skin parasite landscape in *Leishmania donovani* infection

Authors

Johannes S. P. Doehl[1¶], Helen Ashwin[1], Najmeeyah Brown[1], Audrey Romano[1#], Samuel Carmichael[2], Jon W. Pitchford[2], Paul M. Kaye[1*]

Affiliations

[1] York Biomedical Research Institute, Hull York Medical School, University of York, York, YO10 5DD, UK

[2] Departments of Biology and Mathematics, University of York, York YO10 5YW, UK.

¶ Current address: Vector Molecular Biology Unit, Laboratory of Malaria and Vector Research, National Institute of Allergy and Infectious Diseases, National Institutes of Health, 12735 Twinbrook Parkway, Rockville, MD 20852, USA

Current address: BILHI Genetics, 60 Avenue André Roussin, 13016, Marseille, France

* Correspondence to: P.M.K. (email: paul.kaye@york.ac.uk)

Abstract

Increasing evidence suggests that infectiousness of hosts carrying parasites of the *Leishmania donovani* complex, the causative agents of visceral leishmaniasis, is linked to parasite repositories in the host skin. However, a detailed understanding of the dispersal and dispersion of these obligatory-intracellular parasites and their host phagocytes in the skin is lacking. Using endogenously fluorescent parasites as a proxy, we apply image analysis combined with spatial point pattern models borrowed from ecology to characterize dispersion of parasitized myeloid cells (including Man^{R+} and $CD11c^{+}$ cells) and predict dispersal mechanisms in a previously described immunodeficient model of *L. donovani* infection. Our results suggest that after initial seeding of infection in the skin, heavily parasite-infected myeloid cells are found in patches that resemble innate granulomas. Spread of parasites from these initial patches subsequently occurs through infection of recruited myeloid cells, ultimately leading to self-propagating networks of patch clusters. This combination of imaging and ecological pattern analysis to identify mechanisms driving the skin parasite landscape offers new perspectives on myeloid cell behavior following parasitism by *L. donovani* and may also be applicable to elucidating the behavior of other intracellular tissue-resident pathogens and their host cells.

38 **Introduction**

39 Vector-borne kinetoplastid parasites of the *Leishmania donovani* complex are the causative
40 agents of zoonotic and anthroponotic visceral leishmaniasis (VL). *Leishmania* parasites occur
41 in two distinct stages; as extracellular promastigotes in their insect vector, hematophagous
42 phlebotomine sand flies (Diptera: Psychodidae: Phlebotominae)[1], and as intracellular
43 amastigotes in the mammalian host[2]. VL is associated with 3.3 million disability-adjusted life
44 years (DALYs)[3] and ~20,000 annual deaths in 56 affected countries[4]. There is no available
45 prophylactic vaccine[5] and available drugs are either expensive and/or show significant
46 toxicity[6].

47

48 Infection of a naïve host with *Leishmania* parasites occurs through the bite of infected sand
49 flies into the skin, the only interface between insect vector and host. *L. donovani* disseminate
50 from the skin to deeper tissues including the spleen, liver and bone marrow causing systemic
51 pathology, but the skin is commonly asymptomatic[7]. Blood parasite load (parasitemia) is
52 considered the main determinant of outward transmission potential and as a surrogate
53 measure of host infectiousness in VL[8]. Other studies, however, point to the importance of the
54 skin as an additional reservoir of parasites. In a recent study[9], the infectiousness of *L.*
55 *donovani*-infected patients in India as measured by xenodiagnoses was found to positively
56 correlate with spleen parasite load as well as blood parasitemia determined by qPCR. Of
57 note, out of 7 infectious patients that remained infectious after drug treatment, 6 had no
58 detectable blood parasitemia[9]. Furthermore, microbiopsy sampling of skin in a VL-endemic
59 region in Ethiopia indicated that parasites can be detected even in asymptomatic individuals,
60 though multiple biopsies from the same patient were often qualitatively and quantitatively
61 different in terms of parasite load[10]. We previously demonstrated in a RAG mouse model of

62 VL that despite high parasite burden in deep tissues, parasitemia was comparatively low
63 (2,000 – 2,500 parasites / ml blood or equivalent to ~2 – 3 amastigotes / blood meal) and not
64 correlated with outward transmission success[11]. Collectively, these data, together with studies
65 in the hamster model of VL[12], in canine VL[13] and in human post-kala azar dermal
66 leishmaniasis[9, 14, 15] support the need to consider skin parasite load as a potential contributor
67 to infectiousness across the disease spectrum attributable to the *L. donovani* complex.
68
69 A confounding feature associated with sampling in many studies relating host infectiousness
70 to skin parasite residence is the possibility of spatial heterogeneity in parasite distribution.
71 Using an immunodeficient model of *L. donovani* infection in mice, we recently demonstrated
72 that obligatory intracellular amastigotes accumulate in patches in asymptomatic host skin,
73 where their dispersion is a strong predictor for the infectiousness of an asymptomatic host[11].
74 However, a detailed understanding of the mechanisms involved in the micro- and macro-
75 scale dispersion of *Leishmania* parasites (and de facto, of parasitized host cells) in the skin is
76 lacking. As a starting point to deciphering these complex processes, we have further
77 exploited the RAG model of VL, where the absence of acquired immune pressure allows
78 underlying innate pathways controlling the dispersion of parasitized myeloid cells to be more
79 clearly studied.
80
81 Here, we describe in detail the micro- and macro-scale dispersion of tandem-dimer Tomato
82 (tdTom) *L. donovani* parasitized cells in the skin of 23 long-term infected RAG mice. Due to
83 the intracellular nature of *Leishmania* amastigotes, their location is equivalent with that of their
84 host cells. Thus, detection of amastigotes can serve as a proxy for detection of parasitized
85 myeloid cells in vivo. We used image analysis tools to extract data based on tdTomato-signal

86 from whole skin images (ImageJ) and also from microscopy images of punch-biopsy skin
87 sections (StrataQuest; see Methods). We then adopted spatial point pattern methodologies
88 from ecology and other fields to interrogate signal dispersion in silico and to make predictions
89 about modes of dispersal[16]. Our results suggest that patches representing infected myeloid
90 cells form “clusters” with a larger patch at the cluster center surrounded by smaller patches.
91 These clusters are consistent with reseeding *L. donovani* amastigotes from a larger patch
92 within a locally varying radius around it. Our data therefore suggest that in the absence of
93 acquired immunity, these patches are the main driver of their own dispersal. This process
94 would also serve to enhance patch growth, as larger patches consist of a merger of smaller
95 patches. This study provides new insights into the complex mechanisms underlying the
96 dispersal and dispersion of *L. donovani*-infected myeloid cells in the skin and exemplifies an
97 approach that may help understand dispersal and dispersion of phylogenetically diverse
98 intracellular pathogens in the skin and other tissues.

99 **Results**

100 *Parasites accumulate in phagocytic cells in the reticular dermis*

101 We generated confocal images of 20 µm thick longitudinal skin biopsy sections from four
102 different RAG mice (RAG19-22). Visual image inspection suggested that *L. donovani*
103 amastigotes resided primarily in the dermis (**Fig. 1A**). For confirmation, two distinct
104 approaches were used. We calculated the shortest distance measurements of individual
105 amastigotes to the epidermis (**Fig. 1B**) and conducted computationally aided amastigote
106 counting in each skin layer (**Fig. 1C**). The former showed that the majority of parasites
107 resided in the reticular dermis, which comprises the deeper 90% of the dermis[17]. The latter
108 showed that the dermis harbored on average ~36x and ~9x more amastigotes / mm^2 than the
109 epidermis and hypodermis, respectively.

110

111 *Leishmania* amastigotes are obligatorily intracellular parasites, residing in phagocytic cells.
112 Not surprisingly, therefore, infected host cells were also found predominantly in the dermis
113 (~29x and ~26x more frequent than in epidermis and hypodermis, respectively; **Fig. 1D**).
114 Thus, parasite dispersion was reflected in host cell dispersion. In fact, the number of
115 parasites / mm^2 skin correlated very strongly with the number of infected cells / mm^2
116 (Spearman r: $P<0.0001$, $r=0.9364$, 95% CI: 0.8432 – 0.9749; **Fig. 1E**), suggesting that the
117 proportion of infected cells increased with the increase in parasite burden.

118

119 In the skin, macrophages and dendritic cells (DCs) are the most abundant phagocytic cell
120 populations in steady state[18]. Alternatively, activated tissue-resident macrophages (TRM2s)
121 expressing the mannose receptor (Man^R) are a preferred host for *L. major* in the mammalian
122 skin[19]. CD11c is a generic DC marker[20], although it can be expressed by tissue macrophages

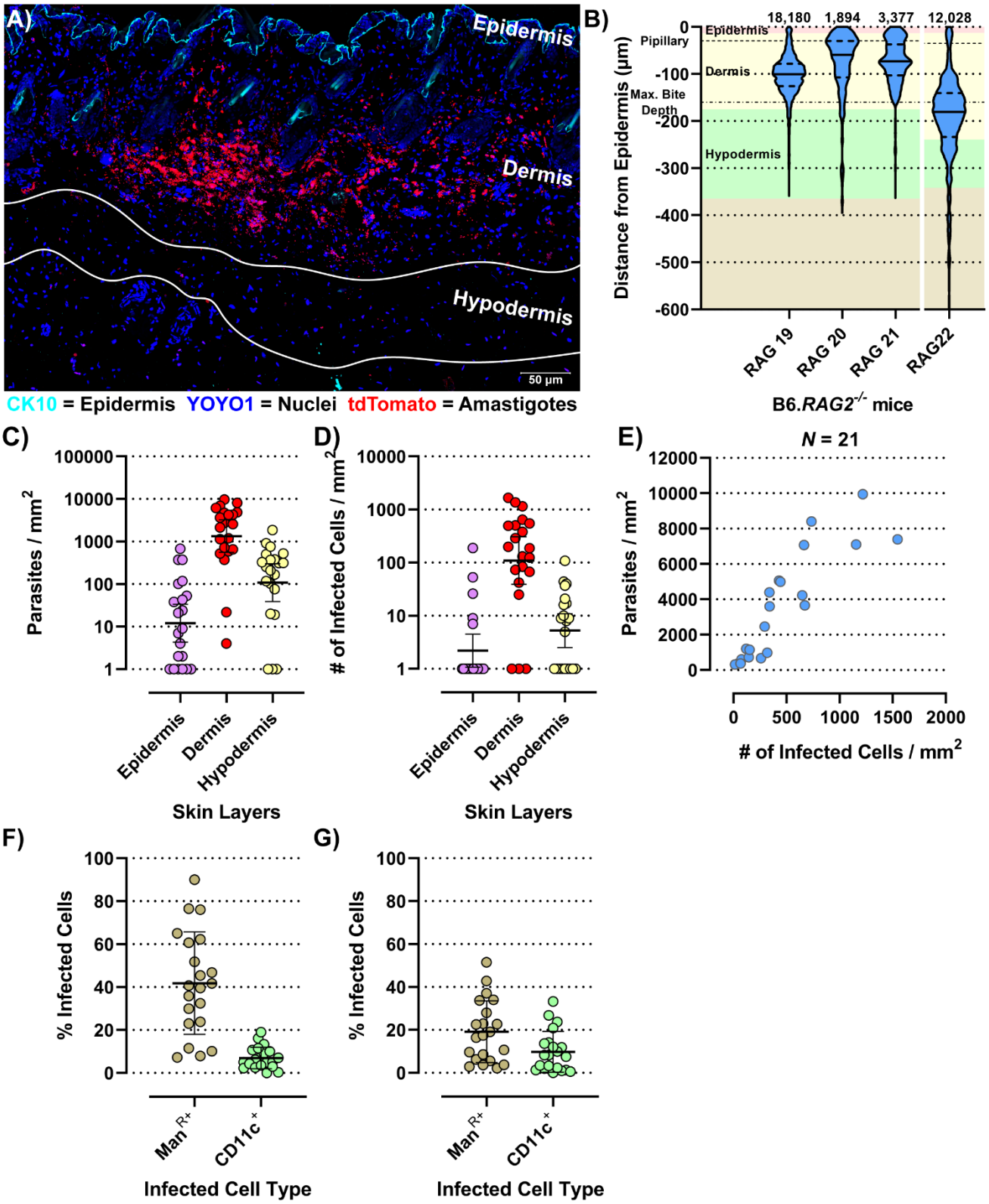
A)
Epidermis
Dermis
Hypodermis
50 µm
CK10 = Epidermis YOYO1 = Nuclei tdTomato = Amastigotes
B)
18,180
1,894
3,377
12,028
Epidermis
Pipillary
Dermis
Max. Bite Depth
Hypodermis
Distance from Epidermis (µm)
0
-100
-200
-300
-400
-500
-600
RAG 19
RAG 20
RAG 21
RAG22
B6.RAG2-/- mice
C)
Parasites / mm2
100000
10000
1000
100
10
1
Epidermis
Dermis
Hypodermis
Skin Layers
D)
# of Infected Cells / mm2
10000
1000
100
10
1
Epidermis
Dermis
Hypodermis
Skin Layers
E)
N = 21
Parasites / mm2
12000
10000
8000
6000
4000
2000
0
0
500
1000
1500
2000
# of Infected Cells / mm2
F)
% Infected Cells
100
80
60
40
20
0
Man R+
CD11c+
Infected Cell Type
G)
% Infected Cells
100
80
60
40
20
0
Man R+
CD11c+
Infected Cell Type

123

124 **Figure 1 | Evaluation of micro-scale parasite distribution in the skin**

125 (A) Representative tile-scan z-stacked confocal microscope image of a 20 μm thick skin biopsy section of the
126 RAG19 mouse. In cyan Cytokeratin-10 (CK-10; epithelium), in blue YOYO-1 (nuclei and kinetoplasts) and in red
127 tdTomato (*L. donovani* amastigotes). The yellow bar is representative of a sand fly proboscis penetrating into the
128 host skin. (B) Violin plot of normalized *L. donovani* amastigote distance from the epithelium. The number of
129 amastigote distances measured are given above each plot. RAG19-21 were female and RAG22 was a male
130 B6.*RAG2*$^{-/-}$ mouse. The background color code for skin layer thickness: pink = epidermis, yellow = dermis, green
131 = hypodermis, tan = subcutaneous tissue. The average sand fly proboscis skin penetration depth is marked by
132 dot-dashed line. (C – M) Evaluation of amastigote localization in the skin. Each circle is representative for a
133 measurement from one of 21 analyzed images across RAG19-22. (C) Parasite counts / skin layer (Friedman
134 test: P<0.0001; Dunn's post hoc test: Epi vs Der: P<0.0001, Epi vs Hypo: P=0.0407, Der vs Hypo: P=0.0047).
135 (D) Counts of infected host cell / skin layer (Friedman test: P<0.0001; Dunn's post hoc test: Epi vs Der:
136 P<0.0001, Der vs Hypo: P=0.0021). (E) Correlation plot of total parasite counts / skin section against all infected
137 cells / skin section (Spearman r: P<0.0001, r=0.8766, 95% CI: 0.7091 – 0.9505). (F) Percent of detected infected
138 Mannose Receptor positive cells of all infected cells compared to detected infected CD11c^{+} cells of all detected
139 infected cells (Paired t-test: P<0.0001, 95% CI: -33.11 to -18.02). (G) Percent of detected infected Mannose
140 Receptor positive cells of all detected Mannose Receptor cells compared to detected infected CD11c^{+} cells of all
141 detected CD11^{+} cells (Paired t-test: P<0.0001, 95% CI: -11.82 to -4.74).

142 under inflammatory conditions[21]. Thus, Man^R and CD11c were used to detect these myeloid
143 cell subsets. We observed that 42% (95% CI: 31% - 52.7%) and 7% (95% CI: 4.7% - 9.3%) of
144 all infected cells were Man^{R+} and $CD11c^+$, respectively (**Fig. 1F**). Thus, while Man^{R+} TRM2s
145 also appear to be permissive host cells for *L. donovani* amastigotes, ~51% of all infected cells
146 detected were neither Man^{R+} or $CD11c^+$. Further, of all Man^{R+} and $CD11c^+$ cells, 19.1% (95%
147 CI: 12.6% - 25.7%) and 9.8% (95% CI: 5.5% - 14.1%) were infected, respectively (**Fig. 1G**),
148 leaving a large proportion of these cells uninfected (~80.9% and ~90.2% of all Man^{R+} and
149 $CD11c^+$ cells, respectively). These data suggest that the observed diverse cellular tropism is
150 not due to saturation of permissive targets such as TRM2s.
151
152 *Patch landscape is sculpted by parasite reseeding and growth*
153 Whole body skins from 23 untreated, tdTom-*L. donovani* long-term infected (6-7 months)
154 RAG mice (Rag1 – 23) were used to analyze the dispersion of skin parasites within their
155 phagocytic host cell. These RAG mice had been used as control mice in seven independent
156 experiments (Exp 1 – 7) and were comparably treated (**Fig. S1A-C**). We used qPCR-based
157 parasite kDNA detection in multiple skin biopsies from each RAG mouse matched against a
158 standard curve to estimate parasite burden per skin biopsy. Comparing parasite burden from
159 biopsies across the skin of each mouse established whether skin parasite burdens varied
160 geographically across the mouse skin and between mice and the mean parasite burden per
161 biopsy per mouse (**Fig. 2A & S2A**). We found considerable variability in mean parasite
162 burden between RAG mice (Kruskal-Wallis Test: $P<0.0001$) and in parasite loads between
163 biopsies from the same RAG mouse (**Fig. S2A**) confirming a heterogeneous parasite
164 dispersion in the host skin[11]. Further, data on the parasite burden per biopsy showed in most
165 cases a departure from a normal distribution for each RAG mouse (Shapiro-Wilks test: see

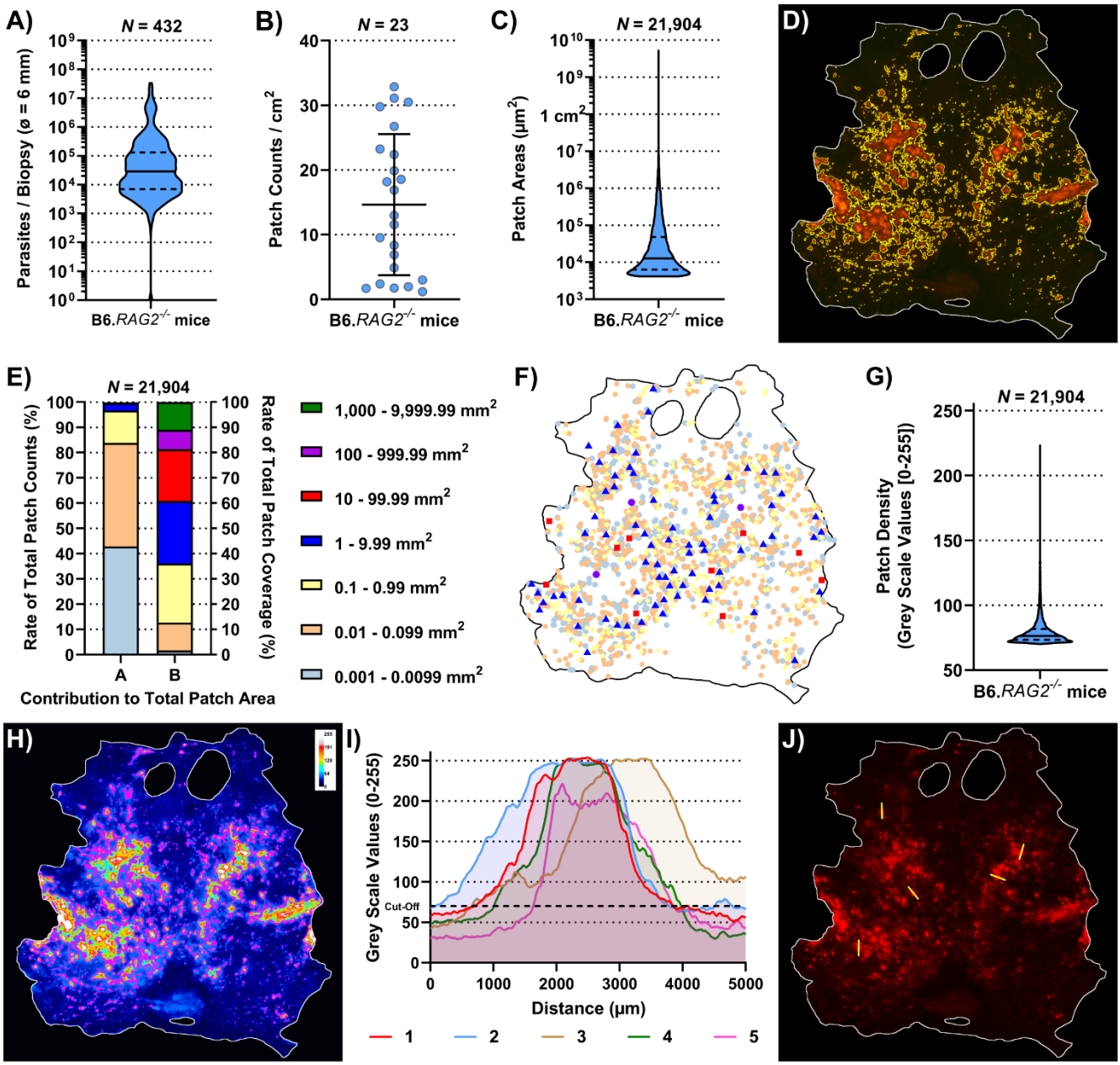
A)
N = 432
Parasites / Biopsy (ø = 6 mm)
B6.RAG2-/- mice
B)
N = 23
Patch Counts / cm2
B6.RAG2-/- mice
C)
N = 21,904
Patch Areas (µm2)
1 cm2
B6.RAG2-/- mice
D)
E)
N = 21,904
Rate of Total Patch Counts (%)
Rate of Total Patch Coverage (%)
Contribution to Total Patch Area
A
B
1,000 - 9,999.99 mm2
100 - 999.99 mm2
10 - 99.99 mm2
1 - 9.99 mm2
0.1 - 0.99 mm2
0.01 - 0.099 mm2
0.001 - 0.0099 mm2
F)
G)
N = 21,904
Patch Density
(Grey Scale Values [0-255])
B6.RAG2-/- mice
H)
I)
Grey Scale Values (0-255)
Cut-Off
Distance (µm)
1
2
3
4
5
J)

166

167 **Figure 2 | Observational description of the skin parasite landscape**

168 (A) Accumulative qPCR data of estimated parasite loads / biopsy from 432 biopsies (ø 0.6 cm) of 23 RAG mice.
169 (B) Average patch counts / cm^2 of skin for 23 RAG mice. (I & K) Comparison of ratios of parasitized skin by body
170 region for 23 RAG mice (Friedman Test: P=03113 & P=0.2931, respectively). (C) Accumulative data of the
171 individual area of 21,904 measured patches from 23 RAG mice. (D) Representative image of detected patches
172 in the RAG4 mouse skin. (E) Arranges data from 21,904 individually detected patches from 23 RAG mice
173 arranged by 'A' the ratio of patch counts / size category and by 'B' the contribution of size category to the overall
174 patched area in the skin. (F) Schematic distribution of patches over the skin of RAG4 marked by patch area
175 according to the categories in (E). (G) Accumulative data of mean patch density / patch of 21,904 individually
176 detected patches from 23 RAG mice. (H) Representative 8-bit grey-scale image showing the tdTomato light
177 intensity per pixel (RAG4). In magenta are the outlines of detected skin patches. (I) X-Y plots of five 5 mm cross
178 sections through patches measuring tdTomato signal intensity / pixel on grey scale [0 – 255] in the RAG4 skin
179 image. The arbitrary cut-off for patch detection set at 70 is marked in these graphs with black dashed line. (J)
180 Image of the RAG4 image indicating where cross sections through patches were made.

181 **Table S1**) and a lack of equal variance (Brown-Forsythe test: P<0.0001). Thus, the median
182 parasite burden per biopsy was used to estimate the total parasite burden in skin for each
183 RAG mouse. In turn, this was used to estimate the mean parasite burden per cm^2 of skin
184 (**Table S1**). Despite intravenous inoculation of equivalent numbers of parasites, there was
185 considerable variability in total parasite burden in skin between RAG mice, ranging from
186 ~$1x10^6$ (RAG12) to $1.24x10^9$ (RAG3) parasites per mouse (**Table S1**).
187
188 Akin to parasite loads, skin patch counts were also highly variable between RAG mice,
189 ranging from ~1.2 patches per cm^2 (Rag14) to ~32.9 patches per cm^2 (Rag8) and 76
190 (RAG14) to 2,457 (RAG10) patches per mouse (**Fig. 2B & Table S1**). We also measured the
191 area of skin patches. Patches measured ~0.00004 cm^2 (50x smaller than a 25G needle prick)
192 to 53 cm^2 (>80% of the mouse skin; **Fig. 2C, D, S3 & Table S1**). Most patches were small
193 (<0.1 mm^2) and only few were large (>1mm^2), resulting in a heavily skewed dataset (**Fig.**
194 **S2B**). More precisely, ~84% detected patches were 0.004 mm^2 – 0.099 mm^2 but accounted
195 for merely ~12.7% of the total patch area (**Fig. 2E**). Conversely, only ~3.3% of detected
196 patches were >1 mm^2 but accounted for ~64% of the total patch area. In an individual mouse,
197 these proportions were even more extreme (**Fig. S4**). In fact, there was a strong correlation
198 between the total patch area and the largest patch in any given mouse (Spearman r:
199 p<0.0001, r=0.9792, 95% CI=0.9496 – 0.9915; **Fig. 3A**). Interestingly, we identified no
200 preferred site of patch accumulation, suggesting that patch dispersion may be random.
201 However, when we plotted patches by size category, we observed that mid- (red and blue
202 symbols; 0.01 – 1 cm^2) and large-range (violet and green symbols; ≥1 cm^2) patches were
203 usually surrounded by several small patches (**Fig. 2F & S5**). Moreover, when focusing on
204 mid-range patch dispersion, these patches appeared to follow unidentified tracks across the

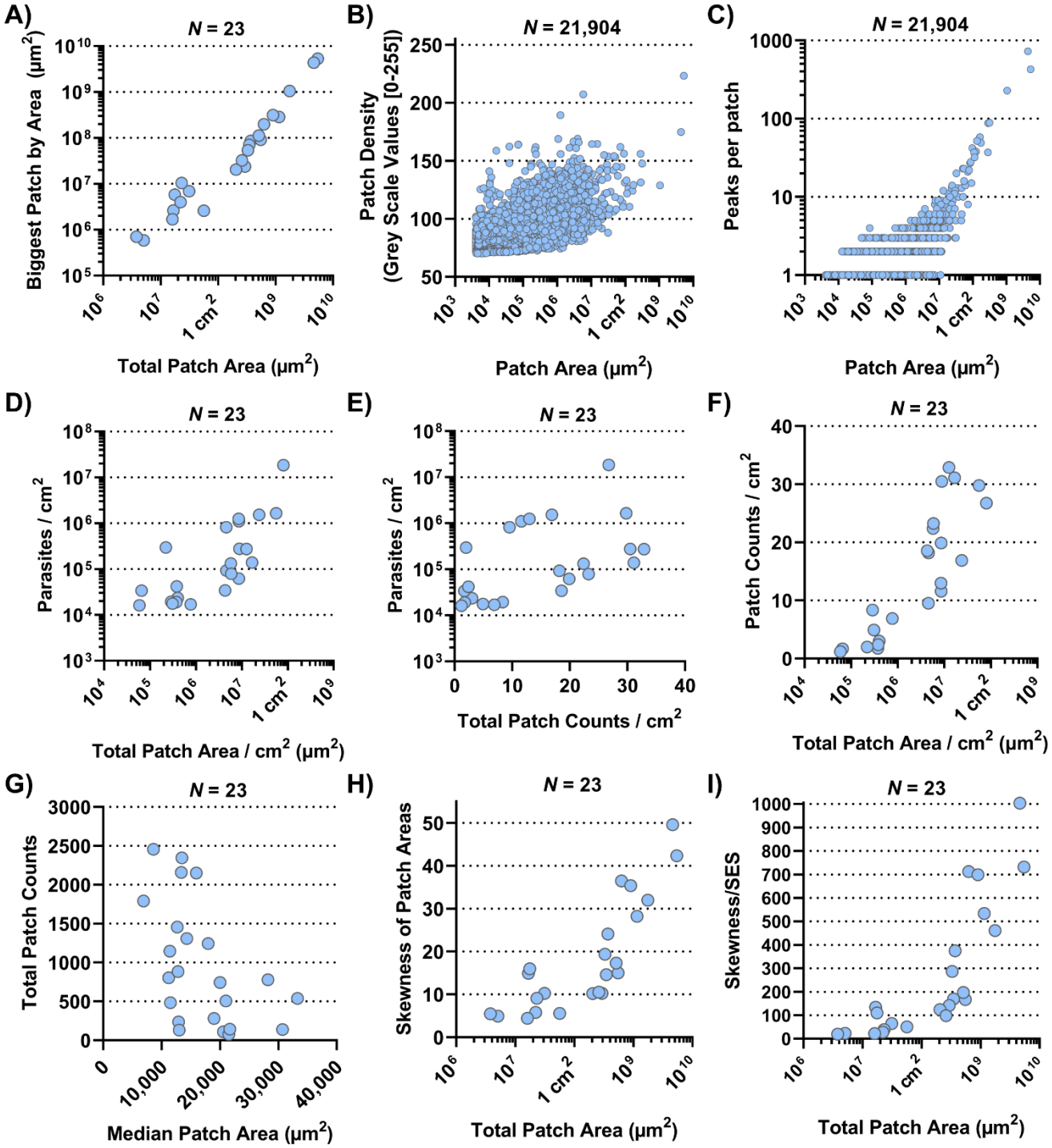
A)
N = 23
Biggest Patch by Area (μm²)
Total Patch Area (μm²)
B)
N = 21,904
Patch Density (Grey Scale Values [0-255])
Patch Area (μm²)
C)
N = 21,904
Peaks per patch
Patch Area (μm²)
D)
N = 23
Parasites / cm²
Total Patch Area / cm² (μm²)
E)
N = 23
Parasites / cm²
Total Patch Counts / cm²
F)
N = 23
Patch Counts / cm²
Total Patch Area / cm² (μm²)
G)
N = 23
Total Patch Counts
Median Patch Area (μm²)
H)
N = 23
Skewness of Patch Areas
Total Patch Area (μm²)
I)
N = 23
Skewness/SES
Total Patch Area (μm²)

205

206 **Figure 3 | Correlation plots**

207 (A) Correlation plot of total parasite patched skin by area (μm^2) against the size of the biggest parasite
208 patch detected in each of the 23 RAG mice (both on a log-scale; Spearman r: $p<0.0001$, r=0.9792, 95%
209 CI=0.9496 – 0.9915). (B) Correlation plot of 21,904 skin parasite patches by area (μm^2) from 23 RAG mice
210 (on a log-scale) against their respective mean pixel density on a 8-bit grayscale (Spearman r: $P<0.0001$,
211 r=0.6554, 95% CI=0.6476 – 0.6631). (C) Correlation plot of 21,904 skin parasite patches by area (μm^2)
212 from 23 RAG mice against the number of high-density peaks per individual patch (both on a log-scale;
213 Spearman r: $P<0.0001$, r=0.3831, 95% CI=0.3714 – 0.3947). (D) Correlation plot of total parasite patched
214 skin by area (μm^2) normalized to 1 cm^2 of skin against parasite burden / cm^2 for each of the 23 RAG mice
215 (both on a log-scale; Spearman r: P $P<0.0001$, r=0.7589, 95% CI=0.4948 – 0.8947). (E) Correlation plot of
216 total skin parasite patch counts normalized to 1 cm^2 of skin against mean parasite burden per punch biopsy
217 for each of the 23 RAG mice (on a log-scale; Spearman r $P=0.0021$, r=0.5741, 95% CI=0.1997 – 0.8022).
218 (F) Correlation plot of total parasite patched skin by area (μm^2) normalized to 1 cm^2 of skin (on a log-scale)
219 against total skin parasite patch counts normalized to 1 cm^2 of skin for each of the 23 RAG mice
220 (Spearman r: $P<0.0001$, r=0.8656, 95% CI: 0.6984 – 0.9432). (G) Correlation plot of the median patch area
221 (μm^2) against total skin parasite patch counts for each of the 23 RAG mice (Spearman r: $P=0.006$, r=-
222 0.5148, 95% CI=-0.7701 to -0.1175). (H) Correlation plot of total parasite patched skin by area (μm^2; on a
223 log-scale) against the skewness of parasite patch area data for each of the 23 RAG mice (Spearman r:
224 $P<0.0001$, r=0.8686, 95% CI=0.7044 – 0.9445). (I) Correlation plot of total parasite patched skin by area
225 (μm^2; on a log-scale) against the test statistic that infers skewness to the population for each of the 23 RAG
226 mice (Spearman r: $P<0.0001$, r=0.9279, 95% CI=0.8311 – 0.9701).

227 skin in several RAG mice (**Fig. S5**). These observations suggested that, while patch
228 dispersion may look different between RAG mice, dispersal is not a random process, but
229 governed by unknown factors in the skin. Our subsequent analysis aimed to test this
230 assertion.
231
232 We observed that patches had higher tdTomato signal at their center compared to their
233 periphery. Since tdTomato amastigotes are approximately of equal brightness, it is
234 reasonable to associate the brighter signal at the patch center with higher amastigote density.
235 A grey-scale pixel analysis in the red channel to measure tdTomato signal intensity per pixel
236 (**Fig. 2H & S6**) showed that most mean grey-scale values per patch were close to the cutoff
237 of 70 (**Fig. 2G, Fig. S2C**). However, when patch area was correlated with their respective
238 average grey-scale value, it showed a strong correlation (**Fig. 3B**; Spearman r: $P<0.0001$,
239 $r=0.6554$, 95% CI=0.6476 – 0.6631). This suggested that as patches grew outward, they
240 became more densely populated with amastigotes. Cross section analysis of tdTomato signal
241 intensity in selected patches showed volcano-like graphs with steep shoulders, suggesting
242 that the amastigote bulk is concentrated at the center of a patch and then thins out quickly at
243 the patch periphery (**Fig. 2I & J**).
244
245 We also observed that larger patches contained multiple areas of high tdTomato-signal (**Fig.**
246 **S6**). Correlating patch area and density peaks per patch suggested that all mid-range and
247 larger patches had multiple density peaks (Spearman r: $P<0.0001$, $r=0.3831$, 95% CI=0.3714
248 – 0.3947; **Fig. 3C**). The statistically weak correlation was explained by the broad base of
249 small patches with only one or two peaks. Accumulation of density peaks per patch only
250 became apparent when patch areas exceeded 1 mm^2 ($>10^6$ μm^2). This suggested that

251 smaller expanding patches grew into one another to form bigger patches. Furthermore, large
252 patches indicated areas where initial parasite seeding had been higher and / or earlier.
253
254 Further, we investigated the relationships between mean parasite burden / cm^2, patch counts
255 / cm^2 and total patch area / cm^2 by correlation plot analysis. Mean parasite burden / cm^2
256 correlated strongly with total patch area / cm^2 of skin, suggesting that increases in total skin
257 parasite burden would also increase total patch area and thus may be the driver of patch
258 growth (**Fig. 3D**; Spearman r: P<0.0001, r=0.7589, 95% CI=0.4948 – 0.8947). Patch counts /
259 cm^2 correlated only moderately with parasite burden / biopsy (**Fig. 3E**; Spearman r:
260 P=0.0021, r=0.5741, 95% CI=0.1997 – 0.8022), suggesting that increases in skin parasite
261 burden was more closely related to patch expansion than new patch seeding. Conversely,
262 when total patch area / cm^2 was correlated with the patch count / cm^2, it showed a very strong
263 positive correlation (**Fig. 3F**; Spearman r: P<0.0001, r=0.8656, 95% CI: 0.6984 – 0.9432),
264 suggesting that the proportion of parasitized host skin is largely determined by the number of
265 observed patches. Correlating the median of patch areas per skin for each RAG mouse to the
266 total patch counts per skin, we found a moderately negative correlation (**Fig. 3G**; Spearman r:
267 P=0.006, r=-0.5148, 95% CI=-0.7701 to -0.1175), which suggested that the more patches a
268 RAG mouse skin had the more of these patches were likely to be small (<0.1 mm^2).
269
270 While data skewness is an underlying characteristic of skin parasite dispersion for any given
271 sample, skewness cannot be directly inferred onto a population. To test whether the observed
272 sample skewness was a general population feature, we divided sample skewness by the
273 standard error of skewness (SES)[22]. The resulting test statistic being outside the interval [-2,
274 2] infers that data skewness was a population property (**Table S1**). For instance, total patch

area per skin was very strongly correlated with the degree of skewness in the patch area data (**Fig. 3H**; Spearman r: P<0.0001, r=0.8686, 95% CI=0.7044 – 0.9445), suggesting that as patchiness increased in the skin, mid-range patches give way to a few large patches surrounded by many small patches. This appears to be a common population feature, given the correlation of the test statistic to the total patch area / skin was even stronger than compared to the sample skewness (**Fig. 3I**; Spearman r: P<0.0001, r=0.9279, 95% CI=0.8311 – 0.9701).

The skin patch landscape is heterogeneously clustered

We previously established that the skin parasite dispersion pertained to concepts of landscape epidemiology[11]. Thus, we applied methodologies of spatial point pattern analysis commonly used in landscape epidemiology to characterize further the dispersion of parasites and their myeloid host cells in skin and identify potential modes of their dispersal[16]. We converted our patch data into spatial point patterns by mapping the center of mass of each patch to a window characterized by the respective RAG skin outline (**Fig. 4A, Fig. S7, Table S2**). After verifying the absence of point duplications, characteristics of patches (e.g. area and density) could optionally be reintroduced to the pattern as a mark (**Fig. 4B, Fig. S8**). Focusing on patch area, we calculated the intensity of point distributions (equivalent to dispersion) with or without a mark and graphically represented the measured point pattern intensities (**Fig. 4C, D, S9 & S10**). Alternatively, we calculated the intensity per cm^2, which is akin to the number of patches per cm^2 and found that both methods corroborated one another (**Table S1 & S2**). As shown in **Figure 4C** (without area mark), intensity showed the distribution of patches by center of mass location, whereas in **Figure 4D** (with area mark) intensity showed the distribution of patches by size in the skin (see also **Fig. S9 & S10**). Both intensities showed a

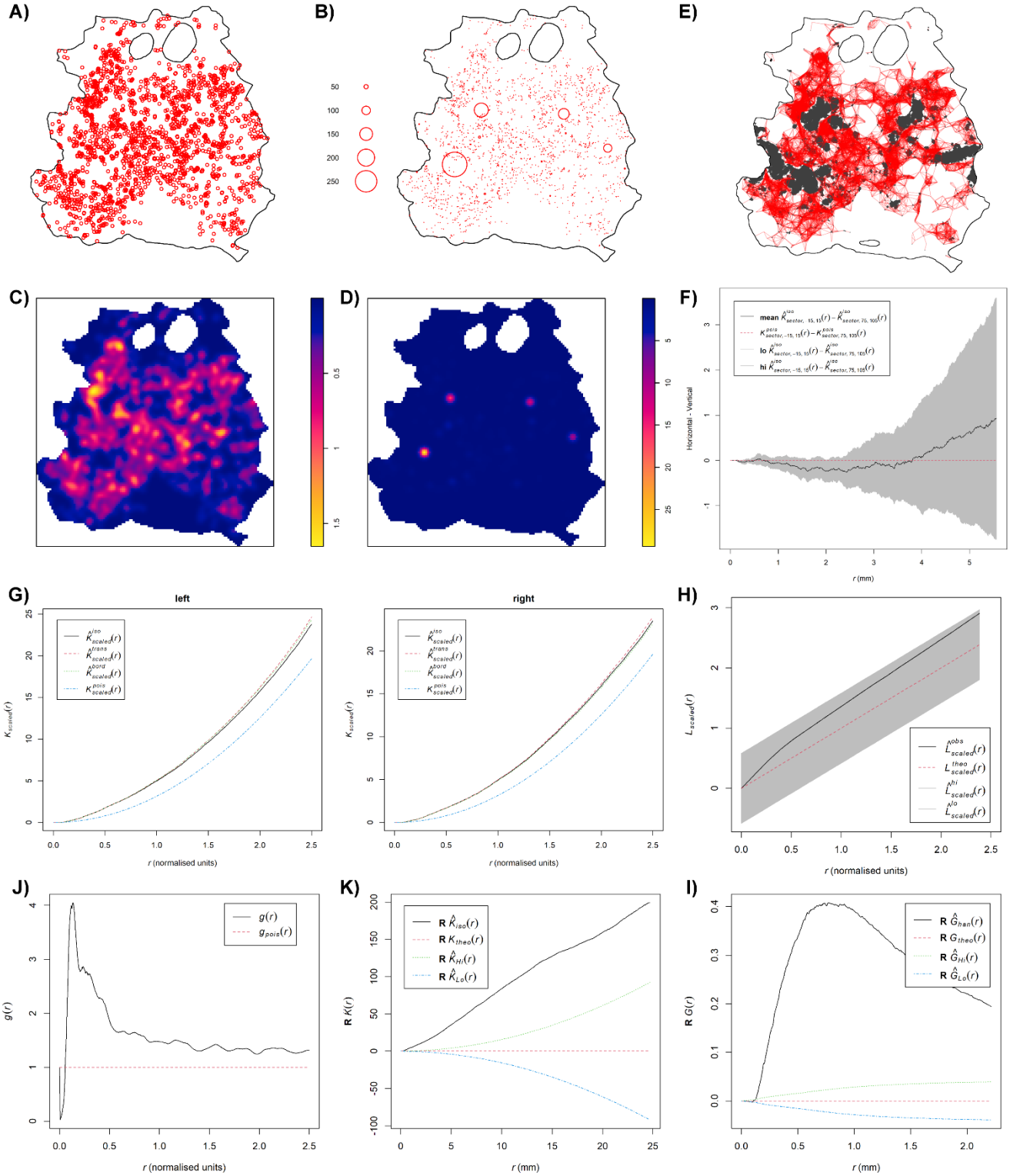
A)
B)
E)
C)
D)
F)
G)
left
right
H)
J)
K)
I)
r (normalised units)
r (mm)
Horizontal - Vertical

299

Figure 4 | Spatial point pattern analysis of skin parasite patch distribution

All graphs are examples for spatial point pattern analysis based on the RAG4 data. (A) Spatial point pattern of skin parasite patches based on center of mass of each detected patch without respective marks. (B) Spatial point pattern of skin parasite patches based on center of mass of each detected patch with respective patch area mark. (C) Patch intensity representation of skin parasite patches based on center of mass of each detected patch without respective marks. (D) Patch intensity representation of skin parasite patches based on center of mass of each detected patch with respective patch area mark. (E) Representation of a cluster analysis output linking all patches whose patch borders are ≤3.9 mm into a network. (F) Graphical representation of the isotropy test showing the theoretical Poisson process (red dotted line), the RAG4 data (black solid line) and the global envelopes (grey). (G) Graphical representation of correlation-stationary test based on a locally scaled K-function. (H) Scaled L-function showing the theoretical Poisson process (red dotted line), the RAG4 data (black solid line) and the global envelopes (grey). (I) Pair correlation function showing the theoretical Poisson process (red dotted line), the RAG4 data (black solid line). (K) Data points independence test based on K-function of the data residuals, showing the theoretical Poisson process (red dotted line), the RAG4 data (black solid line) and the upper (green) and lower limits (blue) of the confidence intervals of the theoretical Poisson process.

315 clear departure from a homogeneous distribution. To gain further understanding of how
316 patches related to one another, we performed a cluster analysis, choosing 3.9 mm as the
317 maximum distance between patch borders (see Methods). This showed small patches
318 clustering strongly around larger patches (**Fig. 4E & S11**), confirming our previous
319 observation from **Figure 2F** (see also **Fig. S5**). Further, this analysis showed the formation of
320 networks of closely clustered patches, which may enhance the likelihood of parasite pick up
321 by a biting sand fly without having to densely parasitize the whole skin (**Fig. 4E & S11**).
322
323 These observations suggested that patch dispersion is likely to be neither homogeneous nor
324 random. To formally test for homogeneity of patch distributions, a quadrat test based on the
325 Fisher's exact test was applied, which rejected homogeneity for all patch distributions
326 (P=0.001; **Table S2**). Thus, an inhomogeneous Poisson point process (IPP) was used as a
327 null hypothesis. Analogue to a homogeneous Poisson point process, an IPP is assumed to be
328 correlation-stationary (the pair correlation between two spots in the window depends only on
329 their relative positions) and isotropic (the distribution is unaffected by the pattern orientation).
330 However, isotropism was rejected for about half of all patch patterns (**Fig. 4F & S12**); RAG14
331 did not produce a reliable test result due to its sparse number of patches. To assess
332 correlation-stationarity, we split the point patterns into two portions of equal numbers of
333 observations and applied the inhomogeneous K-function, which is derived from Ripley's K-
334 function, to each half of the pattern. The analysis showed considerable disagreement
335 between the two plots for several mice indicating that the whole point pattern was not
336 correlation-stationary (**Fig. S13**). In addition, the inhomogeneous K-function showed
337 considerable disagreement between different applied border corrections, which suggested
338 that an IPP was a bad fit to describe patch patterns. In addition, we rejected a Poisson

339 distribution for our patch patterns based on a Quadrat Count test (**Table S2**). These
340 disagreements suggested that the spatial scale of point interactions, which is assumed to be
341 constant by the inhomogeneous K-function[16], was locally variable for our patch patterns.
342 Thus, by assuming a point process that was locally stationary and isotropic but showed a
343 varying rescaling factor between locations in the skin, we could use a locally scaled K-
344 function to rerun the correlation-stationary test. Although not perfect, agreement between the
345 two plots per mouse and between different border corrections was significantly improved (**Fig.**
346 **4G & S14**), suggesting that patch distribution was locally scaled.
347
348 We proceeded with the scaled L-function, derived from Besag's L-function, to determine if
349 patches were evenly spaced (regular), randomly spaced (independent) or clustered (**Fig. 4H**
350 **& S15**). While the fitted data (black solid line) generally departed from the hypothetical
351 random distribution toward a clustered one (black solid line above dotted red line), only
352 RAG11, RAG13, RAG14 and RAG23 showed a clear departure from the global simulation
353 envelops of a hypothetical random distribution (grey shaded area) toward clustering. To
354 confirm these results, we used the pair correlation function (PCF). The scaled PCF analysis
355 showed for most mice, patch patterns departed from the theoretical random distribution
356 (dotted red line) toward a clustered point process (black line above the red dotted line), in
357 particular, at short distances between patches (**Fig. 4J & S16**). With increased distances
358 between patches, some point patterns showed an approximation to more point
359 independence. Applying the K- and nearest-neighbor (G-) function to the point pattern
360 residuals showed a clear departure of independence toward clustering at shorter distances,
361 indicating positive point dependence (black line outside the upper confidence intervals [dotted
362 green line]) for both tests (**Fig. 4K, L, S17 & S18**).

363

364 *Modelling the point process behind patch patterns suggests influence of covariates*

365 Consequently, to model patch distribution we adopted a model that accounted for positive
366 point (patch) dependence (clustering) and was tolerant to a locally varying distribution scale.
367 We used different cluster processes (Cauchy, Matérn, Thomas and Variance-Gamma) as
368 described by a Baddeley et al. ('spatstat'[16]) that assume that cluster formation is based on a
369 parental point distribution that seeded the observed points around themselves within a radius,
370 which is variable between clusters due to the locally scaled nature of cluster distribution. This
371 assumption is reflected in our data showing that small patches cluster around mid-range and
372 large patches (**Fig. 2F, 4E, S5 & S11**).

373

374 13 of the 23 patch distributions were best fitted by a Matérn cluster process, while the other
375 10 were best fitted by a Thomas cluster process. The Matérn cluster process assumes a
376 uniform distribution of offspring around the parental point, while the Thomas cluster process
377 assumes offspring to be randomly displaced from the parental point[16]. Checking the
378 parameters selected by the model showed that they were within a reasonable range,
379 confirming model validity (**Table S3**). This was further confirmed by the scaled L-function of
380 the selected fitted models for each patch pattern (**Fig. 5A & S19**). The L-functions of the fitted
381 models closely resembled the L-functions from the point pattern analyses (**Fig. 4H & S15**).
382 Further, we used the selected fitted models to run 4 simulations each to see if the outcome
383 would resemble the distributions the original data (**Fig. 5B & S20**). With a few exceptions,
384 like RAG3, the simulation outputs provided a good representation of the original patch
385 dispersion data (**Fig. 4A & S7**).

386

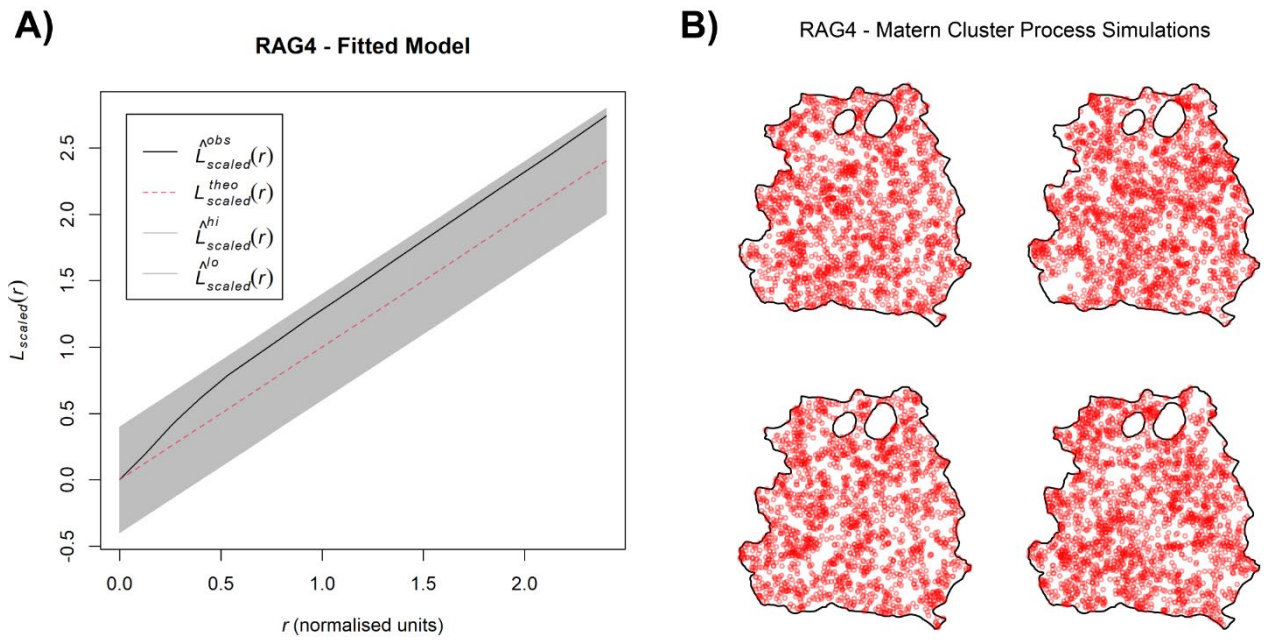

Figure 5 | Basic model evaluation of skin parasite patch distribution

(A) Scaled L-function showing the theoretical Poisson process (red dotted line), the RAG4 predicted model data (black solid line) and the global envelopes (grey). (B) Four model simulations based on the Matérn cluster process for RAG4.

392 Based on these findings, we can deduce how the dispersal of parasites and their myeloid
393 host cells may operate. Both the Matérn and Thomas cluster processes assume points of
394 origin that seed new points within a set radius to create an observed clustered point
395 dispersion. In a locally scaled setting, as it is the case for our patch distribution, this radius is
396 locally varying in length and thus distinct for each patch cluster. Analogously, after initial skin
397 infection, the dispersal of patches may be explained by existing patches locally seeding new
398 patches around themselves, while growing outward, creating a self-propagating network of
399 patch clusters in the skin (**Fig. 6 & S21**).

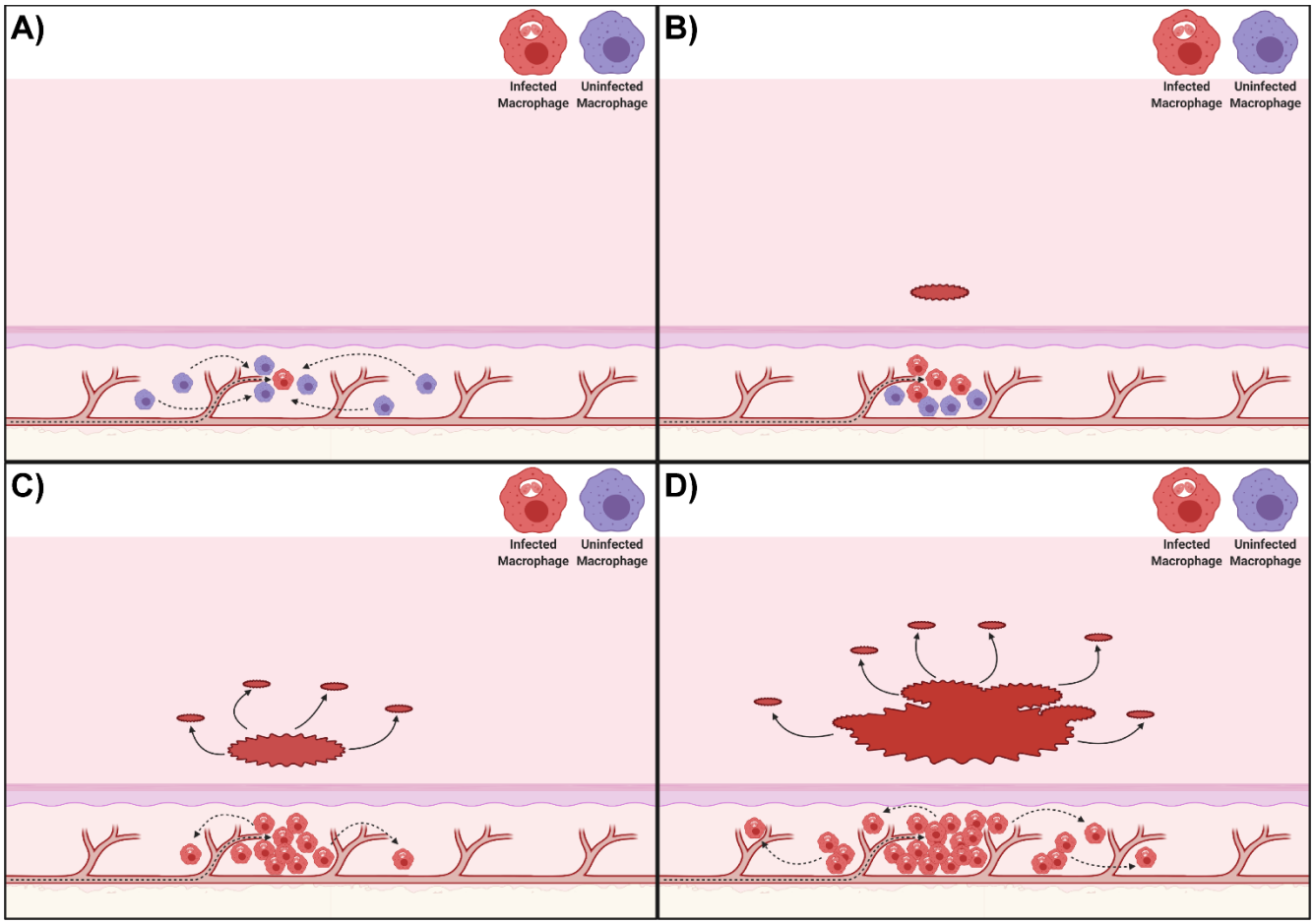

Figure 6 | Proposed mechanism for the dispersal of patches of *L. donovani*-infected myeloid cells

(A) After an initial *Leishmania* amastigote seeding event in the skin e.g. by arrival of an infected myeloid cells (in red) from the circulation, uninfected phagocytic cells (in purple) in the skin are attracted to the infected cells to form a type of innate granuloma. (B) Uninfected myeloid cells are gradually infected in the innate granuloma forming a patch of infected myeloid cells. (C) As these patches keep growing, they seed new patches within a radius ‘r’ around themselves, potentially by escape of infected myeloid cells or via transient release of free amastigotes. (D) This process then keeps repeating itself, forming self-propagating networks of patch “clusters”. All images were created with BioRender.com.

409 **Discussion**

410 It is known that heterogeneity in skin parasite dispersion provides a mechanism to enhance
411 host infectiousness to sand fly vectors[11]. Here we have provided evidence for the underlying
412 mechanisms driving this heterogeneity. To our knowledge, this is the first study to make use
413 of spatial point pattern methodologies[16] in this way. The Matérn and Thomas cluster
414 processes, which were identified to best describe how dispersion of patches of parasites and
415 their infected myeloid host cells occurred, both assume points of origin which seed new points
416 within locally varying radii clustering around them. Based on this analysis, we therefore
417 propose that existing patches locally seed new patches around themselves, giving rise to
418 patch clusters with a central large patch. Since patches are densely parasitized, these patch
419 networks would increase the chance of high parasite loads being acquired by a sand fly and
420 eliminate the need for parasitism of the entire skin. Indeed, our conservatively chosen
421 tdTomato-signal and patch size thresholds may underestimate very small patches leading to
422 patch networks that are denser than reported here, further enhancing outward transmission
423 potential.

424

425 In vivo, *Leishmania* amastigotes reside in phagocytic cells in the dermis, primarily
426 macrophages[23]. Therefore, parasite dispersion is linked to host cell dispersion, a subject on
427 which scant information is available. In the steady-state dermis, macrophages and DCs are
428 the primary phagocytic cell populations[18]. Interestingly, macrophages and DCs have very
429 particular distributions in steady-state skin. Branched DCs are predominantly interstitially
430 localized directly underneath the dermal-epidermal junction[24, 25]. Macrophages are commonly
431 found below these DCs; mostly interstitially. Deeper in the reticular dermis, both cell types
432 associate perivascular to blood vessels rather than lymphatic vessels and DCs here are more

433 rounded. Among the different macrophage populations in the skin, it was shown that Man^{R+}
434 TRM2s are important as long-term *L. major* host cells[19]. In addition, the rate of parasite
435 infection in Man^{R+} TRM2s (~45%) correlated strongly with the severity of skin pathology and
436 parasite survival in the host. The rate of infection in DCs was much lower (22.5%), indicating
437 a preference of *L. major* for Man^{R+} TRM2s[19]. In our study, the observed infection rates for
438 both cell types with *L. donovani* were less than half of this (~19.1% and 9.8%, respectively),
439 but *L. donovani* similarly showed a preference for Man^{R+} TRM2s over DCs (5:1). These cells
440 constituted almost 50% of all infected host cells. Conversely, 50% of host cells belonged to
441 neither group; presumably, other myeloid-derived phagocyte populations[23]. Interestingly, the
442 majority of Man^{R+} TRM2s and CD11c^{+} DCs (~80.9% and ~90.2%, respectively) were
443 uninfected in the analyzed skin sections, despite the high number of parasites present in
444 some of the sections. This raised the question of why the small proportion of infected host
445 cells should be clustered close together and also indicates that observed cellular tropism is
446 not due to saturation of preferred targets.
447
448 Further, our analysis suggested that the process of forming patches may be influenced by
449 yet-to-be-identified covariates. One covariate may be proximity to blood vessels as Man^{R+}
450 TRM2s often colocalize to them in the dermis, where they can pick up macromolecules from
451 the blood[19, 26]. Given that parasitized phagocytic cells in circulation may have properties
452 associated with apoptotic cells[27], it is possible that TRMs capture parasitized host cells by
453 efferocytosis, thus seeding new skin sites for patch formation. Alternatively, infected
454 phagocytes in circulation could exit the vasculature by extravasation at sites of sub-clinical
455 inflammation. Either mechanism could explain why mid-range patch distribution appeared to
456 follow unidentified lines in the skin and why there was no preferred location for parasite

457 accumulation in the skin. Further, proximity to blood vessels may also enhance access to
458 nutrients from the circulation for parasitized phagocytic cells and thus, indirectly promote
459 parasite proliferation. Also, parasite proximity to blood vessels would improve their chances to
460 be found by a probing sand fly. Future analysis could potentially confirm blood vessel
461 association of parasite patches by proximity measurements. Three-dimensional (e.g. light
462 sheet) microscopic imaging data would be needed to achieve this. This and other covariates
463 that may affect the establishment of parasite niches can be integrated in the future into the
464 Matérn and Thomas cluster process models to determine their influence on the dispersal and
465 dispersion of parasites and their myeloid host cells.
466
467 Independent of the means of initial skin seeding of parasites, our data indicate that the
468 accumulation of infected myeloid cells into patches could be analogous mechanistically to
469 phagocyte migration during granulomatous inflammation. For example, early in the process of
470 *L. donovani*-dependent granuloma formation in the liver, uninfected Kupffer cells (KCs)
471 migrate towards a granuloma-initiating infected KC resulting in a heterogeneous distribution
472 of KCs and their condensation and subsequent infection at the granuloma core[28, 29].
473 Conversely, studies in zebrafish embryos infected with *Mycobacterium marinum* highlight the
474 innate capacity of phagocytes to exit granulomas[30], an innate feature of the phagocytic cell
475 response to infection that appears to be obscured in fully immunocompetent mouse models of
476 granulomatous inflammation[28]. Our RAG mouse model of skin infection similarly lacks the
477 confounding effects of an adaptive immune response, providing a similarly unique window on
478 processes driving innate myeloid cell aggregation and a platform on which to build increasing
479 levels of immune complexity. It remains to be determined to what extent patches form
480 because of the inherent migratory properties of phagocytic cells and / or modification of such

481 properties by intracellular amastigotes. Manipulation of phagocyte function by intracellular
482 *Leishmania* has been well-described[31] though few studies have addressed phagocyte
483 migratory potential. Similarly, whilst phagocyte heterogeneity in skin is well described (see
484 above), the mechanisms regulating mobility of these cells is their natural 3D-environment
485 remain poorly understood.
486
487 The notion that new patches are seeded primarily from existing patches is supported by the
488 observation that larger patches were surrounded by smaller patches that emerged within
489 limited distances from the larger patches, resulting in patch clustering. If, akin to parasite
490 dispersion, parasite dispersal is also linked to its host cells, then, mechanistically, patch
491 clustering could occur by escape of infected host cells from these “innate granuloma”-like
492 parasite patches as was demonstrated in *M. marinum*-infected zebrafish embryos[32].
493 Conversely, parasites could be redistributed to uninfected host cells within a limited radius
494 from patches by amastigote release from ruptured host cells or by intercellular passage.
495 Macrophages are known to form a variety of open-ended tunneling nanotubes (TNT) between
496 one another at a distance and such structures have been implicated in the spread of several
497 respiratory viruses and HIV-1[33, 34, 35]. We know of no formal evidence, however, to show that
498 *Leishmania* parasites are transported between macrophages via TNTs.
499
500 The cores of patches are very dense with parasites and heavily infected host cells, but the
501 patch fringes are much less heavily parasitized, suggesting that parasites proliferating
502 strongly within a patch are then pushed outward. Mandell & Beverley (2017) observed that
503 not all amastigotes in the host skin proliferate at the same rate and described two distinct
504 amastigote populations; one that was dormant, the other proliferative[36]. Thus, patches may

505 represent areas of where amastigotes are proliferative, while inter-patch space could mark
506 areas of dormant amastigotes. Whether host cell metabolism stimulates/supports amastigotes
507 to proliferate in the mammalian host skin[37], remains to be determined.
508
509 In summary, through spatial point pattern analysis combined with systematic image analysis
510 we provide a novel mechanistic framework to explain how the dispersal of *L. donovani*
511 infected myeloid cells occurs in the absence of the constraints imposed by acquired immunity.

512 **Materials and Methods**

513 *Ethics statement*

514 All animal usage was approved by the University of York Animal Welfare and Ethics Review
515 Committee and the Ethics Review Committee at FERA Science Ltd., and performed under
516 UK Home Office license ('Immunity and Immunopathology of Leishmaniasis' Ref # PPL
517 60/4377).

518

519 *Mouse, Leishmania and sand fly lines*

520 C57BL/6 CD45.1.*Rag2*$^{-/-}$ (RAG) mice (originally obtained from the National Institute of Medical
521 Research, London, UK) were used. All animals were bred and maintained at the University of
522 York according to UK Home Office guidelines. The Ethiopian *Leishmania (Leishmania)*
523 *donovani* strain (MHOM/ET/1967/HU3) had been transfected with a tdTom gene[38] to generate
524 a tdTom-*L. donovani* line in another study[29]. The parasites were maintained RAG mice by
525 repeat-passage of amastigotes. For both parasite passage and RAG mouse infection, tdTom-
526 *L. donovani* amastigotes were isolated from the spleens of long-term infected RAG mice and
527 i.v. at $8x10^7$ amastigotes / uninfected RAG mouse as previously described[11].

528

529 *Mouse skin harvest*

530 All animals were untreated control animals pooled from 7 different experiments. All animals
531 were exposed to comparable experimental conditions (**Fig. S1A & B**). Mouse skin harvest
532 was performed as previously described[11]. Briefly, RAG mice were sacrificed in a CO_2-
533 chamber, followed by cervical dislocation. Animals were first shaven with electric clippers and
534 then treated with a depilation cream (Veet by Reckitt, Slough, UK) for up to 3 min. The
535 depilation cream was scraped off and residual cream was washed off under running water.

536 Mice were skinned by an abdominal double-Y incision, removal of ears and exclusion of paws
537 and tail (**Fig. S1C**). The skin was pulled from the rump over the head and then cut off at eye-
538 level. Excess adipose tissue was removed with curved tweezers and skins were kept in
539 complete RPMI on ice until stereomicroscopic imaging and subsequent biopsy punching.
540
541 *Genomic DNA extraction*
542 16 or 24 skin biopsies (ø 0.6 cm) were taken from each skin as previously described[11]. All
543 genomic DNA (gDNA) extractions were performed with either the DNeasy® Blood & Tissue
544 spinning column kit (Qiagen, Venlo, Netherlands) or the DNeasy® 96 Blood & Tissue plate kit
545 (Qiagen) according to supplier's protocol.
546
547 *Quantitative Polymerase Chain Reaction*
548 All quantitative real-time PCRs (qPCR) were performed as previously described[11]. Briefly,
549 previously characterized *Leishmania*-specific kinetoplastid DNA primers (Accession number
550 AF103738)[39] were used at a final concentration of 200 nM. 2 ng of total gDNA extracted from
551 skin biopsies were used / reaction. Fast SYBR® Green Master Mix (Applied Biosystems) was
552 used according to supplier's guidelines. Reactions were run in a StepOnePlus™ thermal
553 cycler (Applied Biosystems, Waltham, MA, USA) with a thermal cycle of 95°C for 20 s, a
554 cycling stage of 40 cycles of 95°C for 3 s, 60°C for 5 s, 72°C for 20 s, 76.5°C for 10 s (data
555 read at final step), followed by the standard melt curve stage. Data was analyzed by
556 StepOne™ Software v.2.3.
557

558 *Microscopy*

559 Fluorescent stereomicroscopy of whole skins was performed as previously described[11].
560 Briefly, a series of 30-40 images at 12x magnification were taken / skin to image the whole
561 skin area from the hypodermal face. All images were taken under the same conditions
562 (exposure time: 400 ms). Image-series were collated in Adobe® Photoshop® to render a
563 single image of the whole mouse skin (Abode Inc., San Jose, CA, USA).

564

565 For confocal microscopy, fixation and cryo-preservation of skin punch biopsies (ø 0.6 cm)
566 was adapted from Accart et al. (2014) to optimize tdTomato-signal and skin integrity
567 preservation after skin freezing and cutting[40]. Skin biopsies were fixed in 2% Formaldehyde in
568 PBS for 15 min at room temperature (RT), rinsed 3x in 15% Sucrose/PBS and incubated
569 overnight at 4°C in a Tris-Zinc fixative (per 100 ml: 1,211.4 mg Tris-base, 501.5 mg $ZnCl_2$,
570 500.5 mg Zinc Acetate Dihydrate, 50.6 mg $CaCL_2$, 15 g Sucrose dissolved in dH_2O) on a
571 shaker. The next day, biopsies were rinsed 3x in 15% Sucrose/PBS and incubated in 7.5%
572 Porcine Gelatine (300 bloom) in 15% Sucrose/PBS in individual cryo-molds at 37°C for 1 h.
573 Biopsies were sealed upright in the gelatine blocks by congealing at RT. Gelatine/specimen-
574 blocks were cut down in size, flash-frozen in isopentane on dry ice, further frozen in OCT in a
575 cryo-mold on dry ice and stored at -80°C. Frozen skin biopsies were longitudinally cut at 20
576 µm thickness to expose all skin layers and section were placed on superfrosted microscopy
577 glass slides. Gelatine was removed by slide incubation in PBS at 37°C for up to 30 min.

578

579 Antibody-labelling of skin sections was adapted from Dalton et al. (2010)[41]. Briefly, slides
580 were rinsed in PBS, permeabilized for 15 min with 0.3% Triton X-100/PBS (perm. buffer),
581 rinsed in PBS, blocked for 30 min with Image-iT™ FX Signal-enhancer (Invitrogen, Waltham,

582 MA, USA), rinsed with PBS and further blocked for 30 min with 5% serum + FcBlock (1:1000)
583 in perm. buffer. Primary antibodies were diluted in 5% BSA in perm. buffer (CK-10 [1 µg/ml]
584 (Abcam: ab76318), Mannose Receptor [1 µg/ml] (Abcam: ab64693), CD11c [5 µg/ml]
585 (Abcam: ab33483)) and incubated with specimen for 90-120 min at RT (Abcam PLC,
586 Cambridge, UK). Slides were washed 3 times in 0.5% BSA/PBS. Secondary antibodies were
587 diluted in 5% BSA in perm. buffer (BV421 [1 µg/ml] [Biolegend: 406410]; Alexa Fluor 647
588 [Invitrogen: A-21451]) and incubated for at least 60 min at RT (BioLegend, San Diego, CA,
589 USA). Slides were washed 2 times in 0.5% BSA/PBS and once in PBS at RT. Specimen were
590 counterstained with 0.2 µM YOYO-1 in PBS for 30 min at RT and washed 2 times in PBS.
591 Slides were mounted in ProLong Gold (ThermoFisher Scientific, Waltham, MA, USA) and left
592 overnight at 4°C. Slides were sealed the next day and imaged with a 40x oil-immersion
593 objective (400x magnification) on a fully motorized invert LSM 880 confocal microscope with
594 Airyscan (Zeiss, Jena, Germany) by z-stacked tile-scanning.
595
596 *Stereomicroscopic image analysis (macro-scale)*
597 All whole-skin images were analyzed with custom-build IJ1 macros in Fiji ImageJ[42]. Whole
598 RAG mouse skins measured 40.4 cm^2 (RAG15) to 82.5 cm^2 (RAG10) in surface area (**Table**
599 **S1**). In comparison, C57Bl.6 mouse skins are negligibly thin, measuring on average 0.034 cm
600 (female) and 0.037 cm (male) in thickness[43]. Thus, we dismiss tissue thickness at the macro-
601 scale and treated whole-skin images as two-dimensional surfaces to simplify the analysis.
602 Patch detection was based on 8-bit grey-scale analysis of the *L. donovani* tdTomato-signal in
603 the isolated red channel. The bright fluorescent signal of densely accumulated amastigotes
604 per host cell strongly enhances the fluorescent-signal far beyond what endogenously
605 fluorescent myeloid cells could have achieve. The obligatory intracellular nature of

606 *Lesihmania* amastigotes allowed us to use the parasite signal as a proxy for infected myeloid
607 cell, which allowed their indirect detection.
608
609 To determine a reliable detection threshold, we applied a three-level approach of the "Multi-
610 Otsu-Threshold" algorithm plugin for Fiji ImageJ to tdTom-*L. donovani* infected and naïve
611 RAG skins[44]. Naïve skins rendered maximum intensity thresholds <35, while infected skin
612 showed a range of about 60-150 on an 8-bit grey-scale. For best detection sensitivity verses
613 specificity balance, we chose a threshold of 70 on an 8-bit grey-scale. Further, we had to
614 define the minimum size of a patch. Best image resolution allowed for a pixel size of 21.47
615 µm x 21.47 µm = 461 μm^2, which did not allow to resolve for individual *L. donovani*
616 amastigote, which are 2 – 3 µm in diameter ($r^2 * \pi = 1.5^2 * 3.1416 \approx 7.1\ \mu m^2$). Within a
617 mammalian host, *L. donovani* amastigotes are intracellular; most commonly residing in
618 macrophages[45]. Thus, *L. donovani* amastigote distribution can be described by their host cell
619 distribution. The cell body shape of macrophages and DCs is plastic and in tissues like the
620 skin highly irregular, making it difficult to calculate the 2D surface area of such cells.
621 Assuming that the overall cell surface is the same between a rounded and irregularly shaped
622 macrophage, accepting an average diameter of 25 µm and assuming a flat cell body shape,
623 we can calculate an approximate 2D cell area ($r^2 * \pi = 12.5^2 * 3.1416 \approx 491\ \mu m^2$)[46]. A single
624 macrophage is therefore defined by at least 4 pixels. We thereby defined the smallest
625 arguable patch size as 2 x 2 macrophages (at least 9 pixels) in 2D. Thus, $(3 * 21.47\ \mu m)^2 =$
626 4148.65 μm^2 was set as the smallest possible size to define patches in our stereomicroscopic
627 images. Using these signal detection and patch size thresholds on naïve RAG skins showed
628 false positive detection of ≤15 small patches (<0.1 mm^2), which could largely be attributed to
629 dust particles and other autofluorescent events (**Fig. S22A**). Further, manual patch counting

630 in 1 cm^2 areas on infected skins was used to assess the false negative detection rate,
631 showing underestimation of very small size (<0.1 mm^2; **Fig. S22B**) and loss of detection
632 sensitivity at larger patch fringes, underestimating patch areas. The macro for density-peak
633 detection was adapted from a publicly available protocol on particle counting in cells (Andrew
634 McNaughton, University of Otago, NZ).
635
636 Further, two standard plugins available for Fiji ImageJ were used; a plugin published by Haeri
637 & Haeri (2015) for nearest neighbor distance (NND) analysis[47] and a plugin published by Ben
638 Tupper to analyze patch clustering[48]. For the latter, a maximum distance of 3.9 mm between
639 patch boarders was chosen. This value was based on the idea that an average sand fly is
640 from proboscis tip to the abdominal posterior about 2 mm long. If we used just <2 mm (1.95
641 mm) as a radius to mark a circular landing zone for sand flies that landing zone has diameter
642 of 3.9 mm (**Fig. S1D**). Conceptually, any patch reaching into the landing zone may be
643 immediately accessible to a sand fly without moving away from its landing spot. Even if a
644 parasite patches bordered just at the periphery of the landing zone, parasites from these
645 patches will end up in the blood pool, which has an average diameter of ~1 mm[11].
646
647 *Confocal image analysis (micro-scale)*
648 Volocity (V.6; Quorum Technologies, Laughton, UK), was used for amastigote to epidermis
649 distance measurements. Individual amastigotes were detected by eroding the tdTomato-
650 signal until signal segments coincided with separate sets of YOYO-1 labelled small nuclei and
651 kinetoplasts. The epidermis was demarcated by consolidating all Brilliant Violet 421 signal of
652 Cytokeratin-10 (CK-10) positive areas into a single mass under exclusion of skin
653 appendages. Distances were measured by taking the shortest distance from the centroid of

654 the tdTom amastigotes to the edge of the CK-10 positive band. To collate distance
655 measurements from images from the same RAG mouse and to compare between RAG mice,
656 the measurements required normalization due variations in skin thickness. We estimated the
657 mean thickness of the epidermis, dermis and hypodermis, respectively, for each image by
658 averaging at least three cross measurements in different places for each layer and then
659 adjusted all measurements by the factor of difference between the mean skin layer thickness
660 and the optical skin thickness as measured by Sabino et al. (2016)[43]. While a difference in
661 sex did not significantly affect the macroscale analysis, at the micro-scale skin shows
662 significant difference between sexes. While epidermal thickness is comparable between male
663 and female C57Bl.6 mice, the dermis of a male C57Bl.6 mouse is ~1.4 times thicker than that
664 of a female. Conversely, the hypodermis of female C57Bl.6 mouse is ~1.84 times thicker than
665 that of a male. Thus male and female B6.*RAG2*$^{-/-}$ mice are not directly comparable.
666
667 StrataQuest (TissueGnostics, Vienna, Austria), was used to measure *L. donovani* amastigote
668 co-localization in and distribution of Man^{R+} and CD11c^{+} cells in the skin. Amastigotes were
669 detected by segmentation on the tdTomato signal and host nuclei were detected by
670 segmentation on a mask of YOYO-1 signal minus tdTomato signal. Host nuclei were used as
671 a seed and a mask expanded based on Brilliant Violet 421 signal of Man^{R} and Alexa Fluor
672 647 signal of CD11c to determine cell type. The epidermis mask was demarcated by
673 consolidating Brilliant Violet 421 signal of Man^{R}, Dylight 650 signal of CD11c and YOYO-1
674 signal areas below the epidermis were excluded by size. Tissue morphology was used to
675 define masks for the dermis and hypodermis. The tissue and cell masks were used to
676 determine the location of the amastigotes.
677

678 *Code availability*

679 All Fiji ImageJ macros and R scripts used in this study were deposited in on GitHub

680 (https://github.com/joedoehl/LeishSkinSPPM) and are freely available for download.

681

682 *Statistics*

683 All statistics were conducted in GraphPad PRISM v.8, SPSS v.25[49] or Rstudio v.1.3.959[50]

684 running R v.4.0.2[51]. Prior to test application, parametric test assumption (normality by

685 Shapiro-Wilk Test; equal variance by Brown-Forsythe test; etc) were tested for all data sets. If

686 these assumptions were not met even after data transformation, appropriate non-parametric

687 tests were selected. In case of the Quadrat test, which is based on chi-squared, chi-squared

688 was replaced by a Fisher's exact test whenever squares of the grid applied to the window of

689 observations had several squares with <5 or at least one square with 0 observations, which

690 was the case for all RAG mice. Prior to statistical analysis, all percent datasets were arcsin

691 transformed. Applied statistical tests are stated throughout the text and in corresponding

692 figure legends. Harvested mouse skins varied considerably in size between RAG mice (40.4

693 cm^2 – 82.5 cm^2). For comparison and correlation analyses between RAG mice, some data,

694 like total patch area, patch counts, parasite counts were normalized to area / cm^2 and counts /

695 cm^2, respectively. Where data skewness was an issue, we used the median as a more robust

696 location measure. Spatial point pattern analysis was performed in Rstudio based on the work

697 of Baddeley and co-workers[16]. The following R packages were used for code execution:

698 abind[52], deldir[53], e1701[54], ggpubr[55], goftest[56], graphics[51], grDevices[51], polyclip[57],

699 RandomFields[58], rlist[59], rms.gof[60], scales[61], sp[62], sparr[63], spatstat[16], spatstat.utils[64], stats[51],

700 tensor[65], tidyverse[66] and utils[51]. Each observation in the analysis was verified by at least two

701 different tests. Running multiple test increases confidence in the result as different tests are
702 not always in agreement.
703
704 *Spatial Point Patterns Methodology*
705 A “spatial point pattern” is a dataset containing the spatial locations of events or objects as
706 points within a window of observation. The characterization of the spatial arrangement of
707 these points is the main focus of spatial point pattern methodologies. This is generally done
708 by measuring inter-point distances and characterizing the dispersion between points. Such
709 methodologies find application in a myriad of fields, including epidemiology, revealing
710 important spatial features not discernable by eye[67]. Of course, not all “point data” permits
711 analysis as a “point pattern”, particularly when sampling location is not relevant to the
712 ultimately studied sample property. Conversely, datasets may represent point patterns which
713 are not immediately recognizable, e.g. when the objects’ physical size exceeds technical
714 classification as points; such limitations can be accommodated by choosing the coordinates
715 of the center of mass of the objects as the point and attaching the objects’ size as an
716 attribute, termed mark, to the respective points[68]. This was used in our study where the size
717 of some observed parasite skin patches clearly exceeds the definition of point objects. Very
718 large skin parasite patches also showed great heterogeneity in tdTomato signal density,
719 containing multiple high-density areas. This suggested that very large skin patches were
720 conglomerates of smaller patches that had coalesced forming continuous, although
721 heterogeneously densely parasitized, patches.
722
723 We used functions provided by the spatstat R package by Baddeley and co-workers[16]. The
724 following definitions are all taken from their work “*Spatial Point Patterns: Methodology and*

Applications with R"[16]. Several functions used in our study were derived from the empirical K-function, originally proposed by Ripley in 1977[69]:

$$\widehat{K}(r) = \frac{|W|}{n(n-1)} \sum_{i=1}^{n} \sum_{\substack{j=1 \\ j \neq i}}^{n} \mathbf{1}\{d_{ij} \leq r\} e_{ij}(r)$$

where d_{ij} is the distance between all ordered paired points x_i and x_j ($d_{ij} = ||x_i - x_j||$), r the value of measured distances ($r \geq 0$), $|W|$ the area of the observation window, $n(n-1)$ the total number pairs of distinct points, 1{…} the 'indicator' notation, which is 1 when statement '…' is true and 0 when false and $e_{ij}(r)$ an edge correction weight. Riley's K-function implicitly assumes that the investigated point process (***X***) has homogeneous intensity and is stationary. If a point process is suspected to be inhomogeneous, then that must be considered in the calculation of the K-function. The standard estimator of *K* can be extended to produce the inhomogeneous K-function:

$$\widehat{K}_{inhom}(r) = \frac{1}{D^p |W|} \sum_{i} \sum_{j \neq i} \frac{\mathbf{1}\{d_{ij} \leq r\}}{\hat{\lambda}(x_i)\hat{\lambda}(x_j)} e(x_i, x_j; r)$$

where $e(x_i, x_j; r)$ is an edge correct weight and $\hat{\lambda}(x_i)$ and $\hat{\lambda}(x_j)$ are estimates of the intensity functions $\lambda(x_i)$ and $\lambda(x_j)$, respectively. The constant D^p is the pth power of

$$D = \frac{1}{|W|} \sum_{i} \frac{1}{\hat{\lambda}(X_i)}$$

The inhomogeneous K-function assumes that the spatial scale of interaction remains constant, while the intensity is spatially varying. However, the spatial scale may be locally dependent. In this case, a rescaled template process may be applied that is locally stationary and isotropic, but shows a varying rescaling factor between locations within the observation window. Thus, the empirical K-function is adjusted for each pair of data points (x_i, x_j) by calculating the rescaled distance

$$d_{ij}^{*} = \frac{||x_i - x_j||}{s(x_i, x_j)}$$

where the rescaling factor is

$$s(x_i, x_j) = \frac{1}{2}\left(\frac{1}{\sqrt{\hat{\lambda}(x_i)}} + \frac{1}{\sqrt{\hat{\lambda}(x_j)}}\right)$$

This means the locally scaled K-function is defined by

$$\widehat{K}_{scaled}(r) = \frac{|W|}{n(n-1)} \sum_{i=1}^{n} \sum_{\substack{j=1 \\ j \neq i}}^{n} \mathbf{1}\{d_{ij}^{*} \leq r\} e_{ij}\,(r)$$

The L-function, as proposed by Besag[69], is then derived from the various K-function by

$$L(r) = \sqrt{\frac{K(r)}{\pi}};\ L_{inhom}(r) = \sqrt{\frac{K_{inhom}(r)}{\pi}};\ L_{scaled}(r) = \sqrt{\frac{K_{scaled}(r)}{\pi}}$$

respectively. The pair correlation function is derived from the K-function as

$$g_h(r) = \frac{K(r+h) - K(r)}{2\pi r h + \pi h^2}$$

When *h* becomes very small, then πh^2 becomes negligible and $\frac{K(r+h)-K(r)}{h}$ becomes the derivative of the K-function with respect to *r* (*K'*(*r*)). Thus, in two dimensions, the pair correlation function can be defined by

$$g(r) = \frac{K'(r)}{2\pi r}$$

More details can be found in Baddeley & co-workers book "*Spatial Point Patterns: Methodology and Applications with R*"[16].

762 *Data availability*

763 The authors declare that the data supporting the findings of the study are available within the

764 article and its Supplementary Information files or are available from the authors upon request.

765 **Acknowledgments**

766 This work was supported by a Wellcome Senior Investigator Award (# WT106203;
767 http://www.wellcome.co.uk) and a MRC Programme Grant (#G1000230;
768 http://www.mrc.ac.uk) to P.M.K. The authors thank Andrew McNaughton from the Confocal /
769 µCT Facility at University of Otago, NZ, for the permission of adapting his protocol and
770 invaluable discussion, Jesus Valenzuela from the VMBU-LMVR at the NIAID/NIH, USA, for
771 encouragement and time made available to complete the manuscript, the Imaging and
772 Cytometry lab and staff, in particular Graeme Park and Jo Marrison, in the Bioscience
773 Technology Facility at the University of York, UK, for use of their equipment and technically
774 knowhow that supported the image acquisition and the staff of the Biological Services Facility
775 at the University of York, UK, for animal husbandry.

776

777 *Author contributions*

778 J.S.P.D. and P.M.K. designed the study; J.S.P.D., H.A., N.B. and A.R. conducted the
779 experimental studies; J.S.P.D. conducted the spatial point pattern analysis, modelling and all
780 the statistical analysis, which were revised by S.C. and J.W.P.; the manuscript was written by
781 J.S.P.D. and P.M.K. and all authors contributed to the final version; P.M.K. supervised the
782 study and has senior authorship; P.M.K. conceived the study.

783

784 *Competing financial interest*

785 There are no competing financial interests in relation to this study.

786 **References**

787 1. Ready PD. Biology of Phlebotomine Sand Flies as Vectors of Disease Agents. *Annual Review*
788 *of Entomology* **58**, 227-250 (2013).

789

790 2. Bates PA. Revising Leishmania's life cycle. *Nat Microbiol* **3**, 529-530 (2018).

791

792 3. Murray CJL*, et al.* Disability-adjusted life years (DALYs) for 291 diseases and injuries in 21
793 regions, 1990–2010: a systematic analysis for the Global Burden of Disease Study 2010. *The*
794 *Lancet* **380**, 2197-2223 (2012).

795

796 4. Alvar J*, et al.* Leishmaniasis Worldwide and Global Estimates of Its Incidence. *PLoS ONE* **7**,
797 e35671 (2012).

798

799 5. Srivastava S, Shankar P, Mishra J, Singh S. Possibilities and challenges for developing a
800 successful vaccine for leishmaniasis. *Parasites & Vectors* **9**, (2016).

801

802 6. Singh N, Kumar M, Singh RK. Leishmaniasis: Current status of available drugs and new
803 potential drug targets. *Asian Pacific Journal of Tropical Medicine* **5**, 485-497 (2012).

804

805 7. Ready P. Epidemiology of visceral leishmaniasis. *Clinical Epidemiology*, 147 (2014).

806

807 8. Miller E*, et al.* Quantifying the Contribution of Hosts with Different Parasite Concentrations to
808 the Transmission of Visceral Leishmaniasis in Ethiopia. *PLoS Neglected Tropical Diseases* **8**,
809 e3288 (2014).

810

811 9. Singh OP*, et al.* Xenodiagnosis to evaluate the infectiousness of humans to sandflies in an
812 area endemic for visceral leishmaniasis in Bihar, India: a transmission-dynamics study. *The*
813 *Lancet Microbe* **2**, e23-e31 (2021).

814

815 10. Kirstein OD*, et al.* Minimally invasive microbiopsies: a novel sampling method for identifying
816 asymptomatic, potentially infectious carriers of Leishmania donovani. *Int J Parasitol* **47**, 609-
817 616 (2017).

818

819 11. Doehl JSP*, et al.* Skin parasite landscape determines host infectiousness in visceral
820 leishmaniasis. *Nat Commun* **8**, 57 (2017).

821

822 12. Valverde JG*, et al.* Increased Transmissibility of Leishmania donovani From the Mammalian
823 Host to Vector Sand Flies After Multiple Exposures to Sand Fly Bites. *J Infect Dis* **215**, 1285-
824 1293 (2017).

825

826 13. Laurenti MD*, et al.* Asymptomatic dogs are highly competent to transmit Leishmania
827 (Leishmania) infantum chagasi to the natural vector. *Vet Parasitol* **196**, 296-300 (2013).

828

829 14. Molina R*, et al.* Infectivity of Post-Kala-azar Dermal Leishmaniasis Patients to Sand Flies:
830 Revisiting a Proof of Concept in the Context of the Kala-azar Elimination Program in the Indian
831 Subcontinent. *Clin Infect Dis* **65**, 150-153 (2017).

832

833 15. Mondal D*, et al.* Quantifying the Infectiousness of Post-Kala-Azar Dermal Leishmaniasis
834 Toward Sand Flies. *Clin Infect Dis* **69**, 251-258 (2019).

835

836 16. Baddeley A, Rubak E, Turner R. *Spatial Point Patterns: Methodology and Applications with R*.
837 Chapman and Hall/CRC Press (2015).

838

839 17. Iglesias-Guitian JA, Aliaga C, Jarabo A, Gutierrez D. A Biophysically-Based Model of the
840 Optical Properties of Skin Aging. *Computer Graphics Forum* **34**, 45-55 (2015).

841

842 18. Dupasquier M, Stoitzner P, van Oudenaren A, Romani N, Leenen PJ. Macrophages and
843 dendritic cells constitute a major subpopulation of cells in the mouse dermis. *J Invest Dermatol*
844 **123**, 876-879 (2004).

845

846 19. Lee SH*, et al.* Mannose receptor high, M2 dermal macrophages mediate nonhealing
847 Leishmania major infection in a Th1 immune environment. *J Exp Med* **215**, 357-375 (2018).

848

849 20. Merad M, Sathe P, Helft J, Miller J, Mortha A. The dendritic cell lineage: ontogeny and function
850 of dendritic cells and their subsets in the steady state and the inflamed setting. *Annu Rev*
851 *Immunol* **31**, 563-604 (2013).

852

853 21. Mai LT, Smans M, Silva-Barrios S, Fabie A, Stager S. IRF-5 Expression in Myeloid Cells Is
854 Required for Splenomegaly in L. donovani Infected Mice. *Front Immunol* **10**, 3071 (2019).

855

856 22. Duncan C. *Fundamental Statistics for Social Research*. Routledge (1997).

857

858 23. Liu D, Uzonna JE. The early interaction of Leishmania with macrophages and dendritic cells
859 and its influence on the host immune response. *Front Cell Infect Microbiol* **2**, 83 (2012).

860

861 24. Wang XN*, et al.* A three-dimensional atlas of human dermal leukocytes, lymphatics, and blood
862 vessels. *J Invest Dermatol* **134**, 965-974 (2014).

863

864 25. Tong PL*, et al.* The skin immune atlas: three-dimensional analysis of cutaneous leukocyte
865 subsets by multiphoton microscopy. *J Invest Dermatol* **135**, 84-93 (2015).

866

867 26. Barreiro O*, et al.* Pivotal role for skin transendothelial radio-resistant anti-inflammatory
868 macrophages in tissue repair. *Elife* **5**, (2016).

869

870 27. Martinez-Lopez M, Soto M, Iborra S, Sancho D. Leishmania Hijacks Myeloid Cells for Immune
871 Escape. *Front Microbiol* **9**, 883 (2018).

872

873 28. Egen JG, Rothfuchs AG, Feng CG, Winter N, Sher A, Germain RN. Macrophage and T cell
874 dynamics during the development and disintegration of mycobacterial granulomas. *Immunity*
875 **28**, 271-284 (2008).

876

877 29. Beattie L*, et al.* Dynamic Imaging of Experimental Leishmania donovani-Induced Hepatic
878 Granulomas Detects Kupffer Cell-Restricted Antigen Presentation to Antigen-Specific CD8+ T
879 Cells. *PLoS Pathogens* **6**, e1000805 (2010).

880

881 30. Davis JM, Clay H, Lewis JL, Ghori N, Herbomel P, Ramakrishnan L. Real-time visualization of
882 mycobacterium-macrophage interactions leading to initiation of granuloma formation in
883 zebrafish embryos. *Immunity* **17**, 693-702 (2002).

884

885 31. Kaye P, Scott P. Leishmaniasis: complexity at the host-pathogen interface. *Nat Rev Microbiol*
886 **9**, 604-615 (2011).

887

888 32. Davis JM, Ramakrishnan L. The role of the granuloma in expansion and dissemination of early
889 tuberculous infection. *Cell* **136**, 37-49 (2009).

890

891 33. Onfelt B*, et al.* Structurally distinct membrane nanotubes between human macrophages
892 support long-distance vesicular traffic or surfing of bacteria. *J Immunol* **177**, 8476-8483 (2006).

893

894 34. Cifuentes-Munoz N, Dutch RE, Cattaneo R. Direct cell-to-cell transmission of respiratory
895 viruses: The fast lanes. *PLoS Pathog* **14**, e1007015 (2018).

896

897 35. Bracq L, Xie M, Benichou S, Bouchet J. Mechanisms for Cell-to-Cell Transmission of HIV-1.
898 *Front Immunol* **9**, 260 (2018).

899

900 36. Mandell MA, Beverley SM. Continual renewal and replication of persistent Leishmania major
901 parasites in concomitantly immune hosts. *Proc Natl Acad Sci U S A* **114**, E801-E810 (2017).

902

903 37. Saunders EC, McConville MJ. Immunometabolism of Leishmania granulomas. *Immunol Cell*
904 *Biol*, (2020).

905

906 38. Shaner NC, Campbell RE, Steinbach PA, Giepmans BNG, Palmer AE, Tsien RY. Improved
907 monomeric red, orange and yellow fluorescent proteins derived from Discosoma sp. red
908 fluorescent protein. *Nature Biotechnology* **22**, 1567-1572 (2004).

909

910 39. Bezerra-Vasconcelos DR, Melo LM, Albuquerque ÉS, Luciano MCS, Bevilaqua CML. Real-
911 time PCR to assess the Leishmania load in Lutzomyia longipalpis sand flies: Screening of
912 target genes and assessment of quantitative methods. *Experimental Parasitology* **129**, 234-
913 239 (2011).

914

915 40. Accart N, Sergi F, Rooke R. Revisiting Fixation and Embedding Techniques for Optimal
916 Detection of Dendritic Cell Subsets in Tissues. *Journal of Histochemistry & Cytochemistry* **62**,
917 661-671 (2014).

918

919 41. Dalton JE*, et al.* Inhibition of receptor tyrosine kinases restores immunocompetence and
920 improves immune-dependent chemotherapy against experimental leishmaniasis in mice. *J Clin*
921 *Invest* **120**, 1204-1216 (2010).

922

923 42. Schindelin J*, et al.* Fiji: an open-source platform for biological-image analysis. *Nat Methods* **9**,
924 676-682 (2012).

925

926 43. Sabino CP*, et al.* The optical properties of mouse skin in the visible and near infrared spectral
927 regions. *J Photochem Photobiol B* **160**, 72-78 (2016).

928

929 44. Liao P-S, Chen T-S, Chung P-C. A Fast Algorithm for Multilevel Thresholding. *Journal of*
930 *Information Science and Engineering* **17**, 713-727 (2001).
931
932 45. Podinovskaia M, Descoteaux A. Leishmania and the macrophage: a multifaceted interaction.
933 *Future Microbiol* **10**, 111-129 (2015).
934
935 46. Guertin DA, Sabatini DM. Cell Size Control. In: *Encyclopedia of Life Sciences*) (2006).
936
937 47. Haeri M, Haeri M. ImageJ Plugin for Analysis of Porous Scaffolds used in Tissue Engineering.
938 *Journal of Open Research Software* **3**, (2015).
939
940 48. Tupper B. Graph Plugin and Demo.) (2010).
941
942 49. Corp. I. IBM SPSS Statistics for Windows.). 25.0. edn. IBM Corp. (2017).
943
944 50. RStudio Team. RStudio: Integrated Development for R.). 1.4 edn. RStudio, PBC. (2020).
945
946 51. R Core Team. R: A language and environment for statistical computing.). 4.0.2. edn. R
947 Foundation for Statistical Computing (2020).
948
949 52. Plate T, Heiberger R. abind: Combine Multidimensional Arrays.). 1.4-5. edn. CRAN (2016).
950
951 53. Turner R. deldir: Delaunay Triangulation and Dirichlet (Voronoi) Tessellation.). 0.1-29. edn.
952 CRAN (2020).

54. Meyer D, Dimitriadou E, Hornik K, Weingessel A, Leisch F. e1071: Misc Functions of the Department of Statistics. (ed E1071) PTGF). 1.7-4. edn. CRAN (2020).

55. Kassambara A. ggpubr: 'ggplot2' Based Publication Ready Plots.). 0.4.0. edn. CRAN (2020).

56. Faraway J, Marsaglia G, Marsaglia J, Baddeley A. goftest: Classical Goodness-of-Fit Tests for Univariate Distributions.). 1.2-2. edn. CRAN (2019).

57. Johnson A, Baddeley A. polyclip: Polygon Clipping.). 1.10-0. edn. CRAN (2019).

58. Schlather M*, et al.* RandomFields: Simulation and Analysis of Random Fields.). 3.3.8 edn. CRAN (2020).

59. Ren K. rlist: A Toolbox for Non-Tabular Data Manipulation.). 0.4.6.1. edn. CRAN (2016).

60. Mukherji S. rms.gof: Root-mean-square goodness-of-fit test for simple null hypothesis.). 1.0. edn. CRAN (2013).

61. Wickham H, Seidel D. scales: Scale Functions for Visualization.). 1.1.1. edn. CRAN (2020).

62. Bivand RS, Pebesma E, Gomez-Rubio V. *Applied spatial data analysis with R*. Springer (2013).

63. Davies TM, Marshall JC, Hazelton ML. Tutorial on kernel estimation of continuous spatial and spatiotemporal relative risk. *Stat Med* **37**, 1191-1221 (2018).

64. Baddeley A, Turner R, Rubak E. spatstat.utils: Utility Functions for 'spatstat'.). 1.17-0. edn. CRAN (2020).

65. Rougier J. tensor: Tensor product of arrays.). 1.5. edn (2012).

66. Wickham H*, et al.* Welcome to the Tidyverse. *Journal of Open Source Software* **4**, (2019).

67. Lessler J, Salje H, Grabowski MK, Cummings DA. Measuring Spatial Dependence for Infectious Disease Epidemiology. *PLoS One* **11**, e0155249 (2016).

68. Ohser J, Muecklich F. Arrangement of Objects. In: *Statistical Analysis of Microstructures in Materials Science*). John Wiley (2000).

69. Ripley BD. Modeling Spatial Patterns. *J Roy Stat Soc B Met* **39**, 172-212 (1977).